
Flow Priors for Linear Inverse Problems via Iterative Corrupted Trajectory Matching

Yasi Zhang
UCLA
yasminzhang@ucla.edu

Peiyu Yu
UCLA
yupeiyu98@g.ucla.edu

Yaxuan Zhu
UCLA
yaxuanzhu@g.ucla.edu

Yingshan Chang
CMU
yingshac@andrew.cmu.edu

Feng Gao*
Amazon
fenggo@amazon.com

Ying Nian Wu
UCLA
ywu@stat.ucla.edu

Oscar Leong
UCLA
oleong@stat.ucla.edu

Abstract

Generative models based on flow matching have attracted significant attention for their simplicity and superior performance in high-resolution image synthesis. By leveraging the instantaneous change-of-variables formula, one can directly compute image likelihoods from a learned flow, making them enticing candidates as priors for downstream tasks such as inverse problems. In particular, a natural approach would be to incorporate such image probabilities in a maximum-a-posteriori (MAP) estimation problem. A major obstacle, however, lies in the slow computation of the log-likelihood, as it requires backpropagating through an ODE solver, which can be prohibitively slow for high-dimensional problems. In this work, we propose an iterative algorithm to approximate the MAP estimator efficiently to solve a variety of linear inverse problems. Our algorithm is mathematically justified by the observation that the MAP objective can be approximated by a sum of N “local MAP” objectives, where N is the number of function evaluations. By leveraging Tweedie’s formula, we show that we can perform gradient steps to sequentially optimize these objectives. We validate our approach for various linear inverse problems, such as super-resolution, deblurring, inpainting, and compressed sensing, and demonstrate that we can outperform other methods based on flow matching. Code is available at <https://github.com/YasminZhang/ICTM>.

1 Introduction

Linear inverse problems are ubiquitous across many imaging domains, pervading areas such as astronomy [41, 23], medical imaging [38, 49], and seismology [35, 39]. In these problems the goal is to reconstruct an unknown image $x_* \in \mathbb{R}^n$ from observed measurements $y \in \mathbb{R}^m$ of the form:

$$y = \mathcal{A}(x_*) + \text{noise}, \quad (1)$$

where $\mathcal{A} : \mathbb{R}^n \rightarrow \mathbb{R}^m$ with $m \leq n$ is a linear operator that degrades the clean image x_* , and the additive noise is drawn from a known distribution. In this work, we assume the noise follows $\mathcal{N}(0, \sigma_y^2 I)$. Due to the under-constrained nature of such problems, they are typically ill-posed, i.e.,

*This work is not related to the author’s position at Amazon.

there are an infinite number of undesirable images that fit to the observed measurements. Hence, one requires further structural information about the underlying images, which constitutes our prior.

With the advent of large generative models [27, 17, 48, 40, 8, 58], there has been a surge of interest in exploiting generative models as priors to solve inverse problems. Given a pretrained generator to sample from a distribution or grant access to image probabilities, one can solve a variety of inverse problems in a task- or forward model-agnostic fashion, without the need for large-scale supervision [36]. This has been successfully done for a variety of models, including implicit generators such as Generative Adversarial Networks (GANs) and Variational Autoencoders (VAEs) [4, 34], invertible generators such as Normalizing Flows [1, 54], and more recently Diffusion models [10, 43, 59].

A recent paradigm in generative modeling [48, 55, 25, 57], based on the concept of flow matching [29, 28], has made significant strides in scaling ODE-based generators to high-resolution images. Flow matching models map a simple base distribution, such as a Gaussian, to a complex, high-dimensional data distribution by defining a flow field that represents the transformation between these distributions. These generative models have demonstrated scalability to high dimensions, forming the backbone of several state-of-the-art generative models [30, 13, 56]. Moreover, flow matching models follow straighter and more direct probability paths compared to diffusion models, allowing for more efficient and faster sampling [28, 29, 13]. Additionally, due to their invertibility, flow matching models provide direct access to image likelihoods through the instantaneous change-of-variables formula [9, 18]. Given these advantages and the relatively recent application of these models to inverse problems [37, 2], we investigate their use as image priors in this work.

Leveraging knowledge about the corruption process $p(y|x)$ and a natural image prior $p(x)$, the Bayesian approach suggests analyzing the image reconstruction posterior $p(x|y) \propto p(y|x)p(x)$ to solve the inverse problem. A proven and effective method based on this approach is maximum-a-posteriori (MAP) estimation [6, 19], which maximizes the posterior to identify the image most likely to match the observed measurements:

$$\operatorname{argmin}_{x \in \mathbb{R}^n} -\log p(x|y) = \operatorname{argmin}_{x \in \mathbb{R}^n} -\log p(y|x) - \log p(x). \quad (2)$$

MAP estimation provides a single, most probable point estimate of the posterior distribution, making it simple and interpretable. This deterministic approach ensures consistency and reproducibility, which are essential in applications requiring reliable outcomes, particularly in compressed sensing tasks such as Computed Tomography (CT) [7] and Magnetic Resonance Imaging (MRI) [52]. While posterior sampling methods can offer diverse reconstructions to quantify uncertainty, they can be prohibitively slow in high-dimensions [5]. Hence, in this work, we propose to integrate flow priors to solve linear inverse problems by MAP estimation.

A significant challenge in employing flow priors for MAP estimation lies in the slow computation of the image probabilities, as it requires backpropagating through an ODE solver [47, 16, 15]. In this work, we show how one can address this challenge via Iterative Corrupted Trajectory Matching (ICTM), a novel algorithm to approximate the MAP solution in a computationally efficient manner. In particular, we show how one can approximately find an MAP solution by sequentially optimizing a novel simpler, auxiliary objective that approximates the true MAP objective in the limit of infinite function evaluations. For finite evaluations, we demonstrate that this approximation is sufficient to optimize by showcasing strong empirical performance for flow priors across a variety of linear inverse problems. We summarize our **contributions** as follows:

1. We propose ICTM, an algorithm to approximate the MAP solution to a variety of linear inverse problems using a flow prior. This algorithm optimizes an auxiliary objective that partitions the flow model’s trajectory into N “local MAP” objectives, where N is the number of function evaluations (NFEs). By leveraging Tweedie’s formula, we show that we can perform gradient steps to sequentially optimize these objectives.
2. Theoretically, we demonstrate that the auxiliary objective converges to the true MAP objective as the NFEs goes to infinity. We validate the correctness of our algorithm in finding the MAP solution on a denoising problem.
3. We demonstrate the utility of ICTM on a wide variety of linear inverse problems on both natural and scientific image datasets, with problems including denoising, inpainting, super-resolution, deblurring, and compressed sensing. Extensive results show that ICTM is both computationally efficient and obtains high-quality reconstructions, outperforming other reconstruction algorithms based on flow priors.

2 Background

Notation We follow the convention for flow-based models, where Gaussian noise is sampled at timestep 0, and the clean image corresponds to timestep 1. Note that this is the opposite of diffusion models. For $t \in [0, 1]$, we denote $x_t(x_0)$ as the point at time t whose initial condition is x_0 . In this work, we use x and x_1 interchangeably, i.e., $x_1(x_0) = x(x_0)$.

2.1 Flow-Based Models

We consider generative models that map samples x_0 from a noise distribution $p(x_0)$, e.g., Gaussian, to samples x_1 of a data distribution $p(x_1)$ using an ordinary differential equation (ODE):

$$dx_t = v_\theta(x_t, t) dt, \quad (3)$$

where the velocity field v is a θ -parameterized neural network, e.g., using a UNet [28, 29, 42] or Transformer [13, 51] architecture. Generative models based on flow matching [28, 29] can be seen as a simulation-free approach to learning the velocity field. This approach involves pre-determining paths that the ODE should follow by specifying the interpolation curve x_t , rather than relying on the MLE algorithm to implicitly discover them [9]. To construct such a path, which is not necessarily Markovian, one can define a **differentiable** nonlinear interpolation between x_0 and x_1 :

$$x_t = \alpha_t x_1 + \beta_t x_0, \quad x_0 \sim \mathcal{N}(0, I), \quad (4)$$

where both α_t and β_t are differentiable functions with respect to t satisfying $\alpha_0 = 0, \beta_0 = 1$, and $\alpha_1 = 1, \beta_1 = 0$. This ensures that x_t is transported from a standard Gaussian distribution to the natural image manifold from time 0 to time 1. In contrast, the diffusion process [48, 45, 20] induces a non-differentiable trajectory due to the diffusion term in the SDE formulation.

The idea behind flow matching is to utilize the power of deep neural networks to efficiently predict the velocity field at each timestep. To achieve this, we can train the neural network by minimizing an L_2 loss between the sampled velocity and the one predicted by the neural network:

$$\mathcal{L}(\theta) = \mathbb{E}_{t, p(x_1), p(x_0)} \|v_\theta(x_t, t) - (\dot{\alpha}_t x_1 + \dot{\beta}_t x_0)\|^2. \quad (5)$$

We denote the optimal (not necessarily unique) solution to $\arg \min_\theta \mathcal{L}(\theta)$ as $\hat{\theta}$. The optimal velocity field $v_{\hat{\theta}}$ can be derived in closed form and is the expected velocity at state x_t :

$$v_{\hat{\theta}}(x_t, t) = \mathbb{E}_{p(x_1), p(x_0)} [\dot{\alpha}_t x_1 + \dot{\beta}_t x_0 \mid x_t]. \quad (6)$$

For convenience, in the following text, we use v_θ to refer to the optimal $v_{\hat{\theta}}$. In the rest of the paper, we assume that the flow v_θ and its parameters are pretrained on a dataset of interest and fixed. We are then interested in leveraging its utility as a prior to solve inverse problems.

2.2 Probability Computation for Flow Priors

Denote the probability of x_t in Eq. (3) as $p(x_t)$ dependent on time. Assuming that v_θ is uniformly Lipschitz continuous in x_t and continuous in t , the change in log probability also follows a differential equation [9, 18]:

$$\frac{\partial \log p(x_t)}{\partial t} = -\text{tr} \left(\frac{\partial}{\partial x} v_\theta(x_t, t) \right). \quad (7)$$

One can additionally obtain the likelihood of the trajectory via integrating Eq. (7) across time

$$\log p(x_t) = \log p(x_\tau) - \int_\tau^t \text{tr} \left(\frac{\partial}{\partial x} v_\theta(x_s, s) \right) ds, \quad 0 \leq \tau < t \leq 1. \quad (8)$$

3 Method

In this work, we aim to solve the MAP estimation problem in Eq. (2) where $p(x)$ is given by a pretrained flow prior. We first discuss in Section 3.1 how the MAP problem could, in principle, be solved via a latent-space optimization problem. As we will see, this problem is challenging to solve

computationally due to the need to backpropagate through an ODE solver. To overcome this, we show in Section 3.2 that the ideal MAP problem can be approximated by a weighted sum of “local MAP” optimization problems, which operates by partitioning the flow’s trajectory to a reconstructed solution. We then introduce our ICTM algorithm to sequentially optimize this auxiliary objective. Finally, in Section 3.3, we experimentally validate that our algorithm finds a solution that is faithful to the MAP estimate in a simplified setting where the globally optimal MAP solution is known.

3.1 Flow-Based MAP

Given a pretrained flow prior, one can compute the log-likelihood of x generated from an initial noise sample x_0 via Eq. (8). Hence, to find the MAP estimate, one could equivalently optimize the initial point of the trajectory x_0 and return $x_1(x_0)$ where x_0 is found by solving

$$\min_{x_0 \in \mathbb{R}^n} \underbrace{\frac{1}{2\sigma_y^2} \|y - \mathcal{A}(x_1(x_0))\|^2}_{\text{data likelihood}} + \underbrace{\frac{1}{2} \|x_0\|^2 + \int_0^1 \text{tr} \left(\frac{\partial}{\partial x} v_\theta(x_t, t) \right) dt}_{\text{prior}}, \quad (9)$$

where $x_t := x_t(x_0)$ denotes the intermediate state x_t generated from x_0 . Intuitively, this loss encourages finding an initial point x_0 such that the reconstruction $x_1 := x_1(x_0)$ fits the observed measurements, but is also likely to be generated by the flow.

In practice, x_1 and the prior term can be approximated by an ODE solver. The trajectory of $x_t = x_0 + \int_0^t v_\theta(x_t, t) dt$ can be approximated by an ODE sampler, i.e. `ODESolve`($x_0, 0, t, v_\theta$), where x_0 is the initial point, and the second and third arguments represent the starting time and the ending time, respectively. For example, with an Euler sampler, we iterate over $x_{t+\Delta t} = x_t + v_\theta(x_t, t) \Delta t$ where $\Delta t = 1/N$ and N is the predetermined NFEs. After acquiring the optimal \hat{x}_0 by optimizing the Eq. (9), we obtain the MAP solution x_1 by using `ODESolve`($\hat{x}_0, 0, 1, v_\theta$) again.

3.2 Flow-Based MAP Approximation

The global flow-based MAP objective Eq. (9) is tractable for low-dimensional problems. The challenge for high-dimensional problems, however, is that optimizing Eq. (9) is simulation-based, and thus each update iteration requires full forward and backward propagation through an ODE solver, resulting in issues regarding memory inefficiency and time, making it hard to optimize [9, 15, 16, 47].

As a way to address this, we prove a result in Theorem 1 that shows that the MAP objective can be approximated by a weighted sum of N local posterior objectives. These objectives are “local” in the sense that they mainly depend on likelihoods and probabilities of intermediate trajectories x_t and $x_t + v_\theta(x_t, t) \Delta t$ for $t = 0, \Delta t, \dots, N \Delta t$ where $\Delta t := 1/N$. Given an initial noise input x_0 , each local posterior objective depends on a non-Markovian **auxiliary path** $y_t = \alpha_t y + \beta_t \mathcal{A}(x_0)$ by connecting the points between y and $\mathcal{A}x_0$. We prove this result for straight paths $\alpha_t = t$ and $\beta_t = 1 - t$ for simplicity, but other interpolation paths can be used. The proof is in Section A.2.

Theorem 1. *For $N \geq 1$, set $\gamma_i := (\frac{1}{2})^{N-i+1}$ and $\Delta t = 1/N$. Suppose $y = \mathcal{A}(x_*) + \epsilon$ where $x_* = x_1(x_0)$ with x_0 being the solution to Eq. (9), $\epsilon \sim \mathcal{N}(0, \sigma_y^2 I)$, and x_t exactly follows the straight path $x_t = tx + (1-t)x_0$ for any timestep $t \in [0, 1]$. Suppose the velocity field $v_\theta : \mathbb{R}^n \times \mathbb{R} \rightarrow \mathbb{R}^n$ satisfies $\sup_{z \in \mathbb{R}^n, s \in [0, 1]} |\text{tr} \frac{\partial}{\partial x} v_\theta(z, s)| \leq C_1$ for some universal constant C_1 . Then, there exists a constant $c(N)^2$ that does not depend on x_0 such that*

$$\lim_{N \rightarrow \infty} \left| \log p(x(x_0)|y) - \sum_{i=1}^N \gamma_i \hat{\mathcal{J}}_i - c(N) \right| = 0,$$

where $\hat{\mathcal{J}}_i = \log p(x_{(i-1)\Delta t}) - \text{tr} \left(\frac{\partial v_\theta(x_{(i-1)\Delta t}, (i-1)\Delta t)}{\partial x} \right) \Delta t + \log p(y_{i\Delta t} | x_{i\Delta t})$.

This result shows that the true MAP objective evaluated at the optimal solution can be approximated by a weighted sum of objectives that depend locally at a time t for the trajectory $\{x_t : t \in [0, 1]\}$. The intuition regarding $\hat{\mathcal{J}}_i$ arises from the fact that $\hat{\mathcal{J}}_i \approx \mathcal{J}_i$, where \mathcal{J}_i is the local posterior distribution

$$\mathcal{J}_i = \log p(y_{i\Delta t} | x_{i\Delta t}(x_{(i-1)\Delta t})) + \log p(x_{i\Delta t}).$$

²This is given by $c(N) := \sum_{i=1}^N \gamma_i c_i - \log p(y)$. Please see the proof of Theorem 1 in Appendix A.2.

Optimizing each of these local posterior distributions in a sequential fashion captures the fact that we would like each intermediate point in our trajectory $x_{i\Delta t}$ to be likely and fit to our measurements, ideally resulting in a final reconstruction x_1 that satisfies this as well. The benefit of $\hat{\mathcal{J}}_i$, as we will show in the sequel, is that it is efficient to optimize.

Discussion of assumptions: We assume that the trajectory $\{x_t\}_t$ exactly follows the predefined interpolation path $\{\alpha_t x + \beta_t x_0\}_t$. In Section B of the appendix, we analyze this assumption and show that we can bound the deviation from the predefined interpolation path to the learned path via a path compliance measure. Moreover, we impose a regularity assumption on the velocity field v_θ , effectively requiring a uniform bound on the spectrum of the Jacobian of v_θ . This can be easily satisfied with neural networks using Lipschitz continuous and differentiable activation functions.

As we see in Theorem 1, one can approximate the true MAP objective via a sum of local objectives of the form

$$\hat{\mathcal{J}}_i := \underbrace{\log p(y_{i\Delta t}|x_{i\Delta t})}_{\text{local data likelihood}} + \underbrace{\log p(x_{(i-1)\Delta t}) - \text{tr} \left(\frac{\partial v_\theta(x_{(i-1)\Delta t}, (i-1)\Delta t)}{\partial x} \right)}_{\text{local prior}} \Delta t. \quad (10)$$

At first glance, $\hat{\mathcal{J}}_i$ still appears challenging to optimize, but there are additional insights we can exploit for computation. We discuss each term in $\hat{\mathcal{J}}_i$ below.

Local data likelihood: The intuition behind ICTM is that we aim to match a **corrupted** trajectory $\{u_t\}_t$ with an auxiliary path $\{y_t\}_t$ specified by an interpolation between our measurements y and $\mathcal{A}(x_0)$ for each timestep t , defined by $y_t := \alpha_t y + \beta_t \mathcal{A}(x_0)$. The corrupted trajectory $u_t := \mathcal{A}(x_t)$ follows the **corrupted flow ODE** $du_t = \mathcal{A}(v_\theta(x_t, t))dt$. To optimize the above ‘‘local MAP’’ objectives, we must understand the distribution of $p(y_t|x_t)$. Generally speaking, this distribution is intractable. However, by assuming exact **compliance** of the trajectory generated by flow to the predefined interpolation path (as done in Theorem 1), we can show that $y_t|x_t \sim \mathcal{N}(u_t, \alpha_t^2 \sigma_y^2)$. This is proven in Lemma 3 in the appendix. While exact compliance of the trajectory may not hold for learned flow matching models, we show empirically that making this assumption leads to strong performance in practice. We further analyze this notion of compliance in Section B of the appendix.

Local prior: The approximation in Eq. (10) addresses one of the main concerns of MAP in that the intensive integral computation is circumvented with a simpler Riemannian sum. This approximation holds for small time increments Δt : $\int_t^{t+\Delta t} \text{tr} \left(\frac{\partial}{\partial x} v_\theta(x_s, s) \right) ds \approx \text{tr} \left(\frac{\partial}{\partial x} v_\theta(x_t, t) \right) \Delta t$. Note that one can additionally improve the efficiency of this term by employing a Hutchinson-Skilling estimate [44, 21] for the trace of the Jacobian matrix. However, at first glance, it appears we have simply shifted the problem to the computation of the prior at timestep $(i-1)\Delta t$. Fortunately, it is possible to derive a formula for the gradient of $\log p(x_t)$ for all timesteps $t \in [0, 1]$ using Tweedie’s formula [12]. This allows us to optimize each objective $\hat{\mathcal{J}}_i$ using gradient-based optimizers. The following result gives a precise characterization of $\nabla_{x_t} \log p(x_t)$, proven in Section A.1.

Proposition 1. *Let $\lambda_t = \alpha_t/\beta_t$ denote the signal-to-noise ratio. The relationship between the score function $\nabla_{x_t} \log p(x_t)$ and the velocity field $v_\theta(x_t, t)$ is given by:*

$$\nabla_{x_t} \log p(x_t) = \frac{1}{\beta_t^2} \left[\left(\frac{d \log \lambda_t}{dt} \right)^{-1} \left(v_\theta(x_t, t) - \frac{d \log \beta_t}{dt} x_t \right) - x_t \right]. \quad (11)$$

In summary, we have derived an efficient approximation to the MAP objective. For our algorithm, we iteratively optimize each term $\hat{\mathcal{J}}_t$ sequentially for each $t = 0, \Delta t, \dots, N\Delta t$, fitting our current iterate x_t to induce an increment $x_{t+\Delta t}$ such that $\mathcal{A}(x_{t+\Delta t})$ fits to our auxiliary corrupted path $y_{t+\Delta t}$ while being likely under our local prior. We call this approach Iterative Corrupted Trajectory Matching (ICTM). Our algorithm is summarized in Algo. 1. In lines 7 and 12, instead of directly optimizing the local data likelihood, we choose λ as a new hyper-parameter to tune. We find a constant λ works well in practice.

3.3 Toy Example Validation

We experimentally validate that the reconstruction found via ICTM is close to the optimal MAP solution in a simplified denoising problem where the MAP solution can be obtained in closed-form.

Algorithm 1 Iterative Corrupted Trajectory Matching (ICTM) with Euler Sampler

Input: measurement y , matrix \mathcal{A} , pretrained flow-based model θ , NFEs N , interpolation coefficients $\{\alpha_t\}_t$ and $\{\beta_t\}_t$, step size η , guidance weight λ , and iteration number K

Output: recovered clean image x_1

```
1: Initialize  $\epsilon \sim \mathcal{N}(0, I)$ ,  $x_0 \leftarrow \epsilon$ ,  $t \leftarrow 0$ ,  $\Delta t \leftarrow 1/N$ 
2: Generate an auxiliary path  $y_s = \alpha_s y + \beta_s(\mathcal{A}x_0)$  for  $s \in (0, 1)$ 
3: while  $t < 1$  do
4:    $x_{t+\Delta t} \leftarrow x_t + v_\theta(x_t, t)\Delta t$ 
5:   if  $t = 0$  then
6:     for  $k = 1, \dots, K$  do
7:        $x_t \leftarrow x_t - \eta \nabla_{x_t} \left[ \lambda \|\mathcal{A}(x_{t+\Delta t}(x_t)) - y_{t+\Delta t}\|^2 + \frac{1}{2} \|x_t\|^2 + \text{tr} \left( \frac{\partial v_\theta(x_t, t)}{\partial x} \right) \Delta t \right]$ 
8:     end for
9:   else
10:    for  $k = 1, \dots, K$  do
11:      # use Eq. (11) to obtain the gradient of  $\log p(x_t)$ 
12:       $x_t \leftarrow x_t - \eta \nabla_{x_t} \left[ \lambda \|\mathcal{A}(x_{t+\Delta t}(x_t)) - y_{t+\Delta t}\|^2 - \log p(x_t) + \text{tr} \left( \frac{\partial v_\theta(x_t, t)}{\partial x} \right) \Delta t \right]$ 
13:    end for
14:  end if
15:   $x_{t+\Delta t} \leftarrow x_t + v_\theta(x_t, t)\Delta t$ 
16:   $t \leftarrow t + \Delta t$ 
17: end while
18: return  $x_1$ 
```

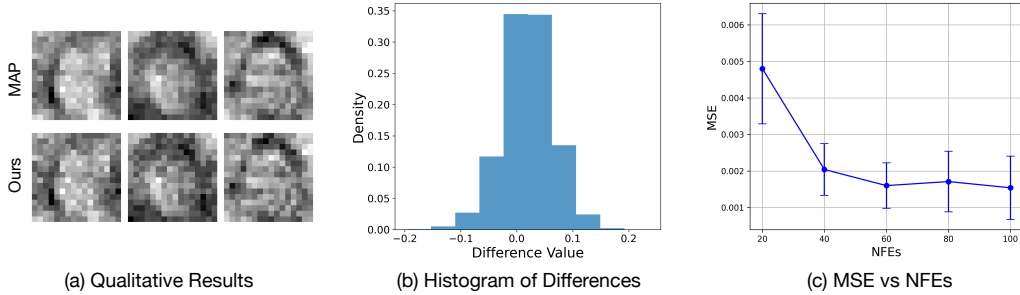


Figure 1: Results of a toy example modeling 1,000 FFHQ faces as a Gaussian distribution. Subfigure (a) shows the qualitative results of our method; Subfigure (b) presents the histogram of the differences between ours and the true MAP; Subfigure (c) displays the MSE values as the NFEs varies.

Specifically, we fit a Gaussian distribution $\mathcal{N}(\mu, \Sigma)$ using 1,000 samples from the FFHQ dataset. Consider a denoising problem $y = x + \epsilon$ where $x \sim \mathcal{N}(\mu, \Sigma)$ and $\epsilon \sim \mathcal{N}(0, \sigma_y^2 I)$. In this case, the analytical solution to the MAP estimation problem (Eq. (2)) is $x_* = (\Sigma^{-1} + \sigma_y^{-2} I)^{-1} (\Sigma^{-1} \mu + \sigma_y^{-2} y)$. We set $\sigma_y = 0.1$. Then, we train a flow-based model on 10,000 samples from the true Gaussian distribution and showcase the deviation of our reconstruction found via ICTM to the closed-form MAP solution x_* in Fig. 1. We see that ICTM can obtain a faithful estimate of the MAP solution across many samples.

4 Experiments

In our experimental setting, we use optimal transport interpolation coefficients, i.e. $\alpha_t = t$ and $\beta_t = 1 - t$. We test our algorithm on both natural and medical imaging datasets. For natural images, we utilize the pretrained checkpoint from the official Rectified Flow repository³ and evaluate our

³<https://github.com/gnobitab/RectifiedFlow>

Table 1: Quantitative comparison results in terms of PSNR and SSIM on the CelebA-HQ dataset. Our algorithm surpasses all other baselines across all tasks. The best values are highlighted in blue and the second-best are underlined.

| Method | Super-Resolution | | Inpainting(random) | | Gaussian Deblurring | | Inpainting(box) | |
|------------------|------------------|--------------|--------------------|--------------|---------------------|--------------|-----------------|--------------|
| | PSNR | SSIM | PSNR | SSIM | PSNR | SSIM | PSNR | SSIM |
| OT-ODE | 27.46 | 0.775 | 28.57 | 0.838 | 26.28 | 0.727 | 19.80 | 0.795 |
| DPS-ODE | 27.85 | 0.791 | 29.57 | <u>0.872</u> | 25.97 | 0.704 | 23.59 | 0.758 |
| RED-Diff | 27.20 | 0.760 | 25.13 | 0.711 | <u>27.23</u> | <u>0.765</u> | 17.50 | 0.651 |
| IIGDM | <u>28.33</u> | <u>0.803</u> | <u>29.98</u> | 0.858 | 24.30 | 0.583 | 24.10 | <u>0.853</u> |
| Ours (w/o prior) | 26.06 | 0.724 | 29.01 | 0.835 | 25.13 | 0.676 | 22.42 | 0.803 |
| Ours | <u>27.91</u> | <u>0.805</u> | <u>30.65</u> | <u>0.894</u> | <u>26.54</u> | <u>0.760</u> | <u>24.34</u> | <u>0.866</u> |

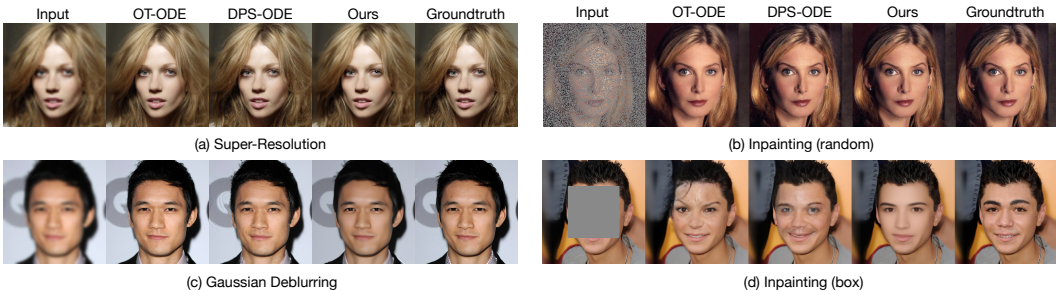


Figure 2: Qualitative comparison results on the CelebA-HQ dataset. The reconstructions generated by our method align more faithfully with the ground truth and exhibit a higher degree of refinement.

approach on the CelebA-HQ dataset [31, 24]. We address four common linear inverse problems: super-resolution, inpainting with a random mask, Gaussian deblurring, and inpainting with a box mask. For the medical application, we train a flow-based model from scratch on the Human Connectome Project (HCP) dataset [50] and test our algorithm specifically for compressed sensing at different compression rates. Our algorithm focuses on the reconstruction faithfulness of generated images, therefore employing PSNR and SSIM [53] as evaluation metrics.

Baselines We compare our method with five baselines. 1) OT-ODE [37]. To our knowledge, this is the only baseline that applies flow-based models to inverse problems. They incorporate a prior gradient correction at each sampling step based on conditional Optimal Transport (OT) paths. For a fair comparison, we follow their implementation of Algorithm 1, providing detailed ablations on initialization time t' in Appendix E.3. 2) DPS-ODE. Inspired by DPS [10], we replace the velocity field with a conditional one, i.e., $v(x_t|y) = v(x_t) + \zeta_t \nabla_{x_t} \log p(y|\hat{x}_1(x_t))$, where ζ_t is a hyperparameter to tune. Following the hyperparameter instruction in DPS, we provide detailed ablations on ζ_t in Appendix E.3. 3) Ours without local prior. To examine the local prior term's effectiveness in our optimization algorithm, we drop the local prior term as defined in Eq. (10) in our algorithm. In the experiments with natural images, in addition to the flow-based baselines, we have included two representative diffusion-based baselines: 4) RED-Diff [33], a variational Bayes-based method; and 5) IIGDM [46], an advanced MCMC-based method. We also note one concurrent work, D-Flow [2], which formulates the MAP as a constrained optimization problem in their Eq. 9. As documented in their Sec. 3.4, it takes 5-10 minutes to recover each image. This is because each of its optimization step requires backpropagation through an ODE solver to compute the full log-likelihood. In contrast, our method is significantly faster (approximately 1.6 minutes per image) due to our principled local MAP approximation, as demonstrated in Appendix D.

4.1 Natural Images

Experimental setup We evaluate our algorithm using 100 images from the CelebA-HQ validation set with a resolution of 256×256 , normalizing all images to the $[0, 1]$ range for quantitative analysis.

Table 2: Results of compressed sensing with varying compression rate ν on the HCP T2w dataset. Note that compressed sensing is more challenging due to the complexity of the forward operator, as evidenced by the poor performance of OT-ODE, which assumes a Gaussian distribution of measurement y given x_t . The best values are highlighted in blue.

| Method | $\nu = 1/2$ | | $\nu = 1/4$ | | $\nu = 1/10$ | |
|---------------|------------------|------------------|------------------|------------------|------------------|------------------|
| | PSNR | SSIM | PSNR | SSIM | PSNR | SSIM |
| Wavelet Prior | 18.02 \pm 1.38 | 0.495 \pm 0.02 | 11.99 \pm 1.34 | 0.230 \pm 0.02 | 7.37 \pm 1.85 | 0.090 \pm 0.02 |
| TV Prior | 25.36 \pm 2.79 | 0.657 \pm 0.04 | 18.70 \pm 2.36 | 0.496 \pm 0.03 | 14.38 \pm 3.04 | 0.309 \pm 0.04 |
| OT-ODE | 18.71 \pm 1.02 | 0.422 \pm 0.17 | 18.16 \pm 1.06 | 0.271 \pm 0.07 | 12.21 \pm 1.43 | 0.096 \pm 0.04 |
| DPS-ODE | 31.06 \pm 3.91 | 0.765 \pm 0.08 | 25.01 \pm 1.87 | 0.608 \pm 0.08 | 22.06 \pm 1.66 | 0.479 \pm 0.09 |
| Ours | 32.72 \pm 1.53 | 0.878 \pm 0.05 | 27.03 \pm 1.77 | 0.733 \pm 0.04 | 24.03 \pm 1.23 | 0.503 \pm 0.04 |

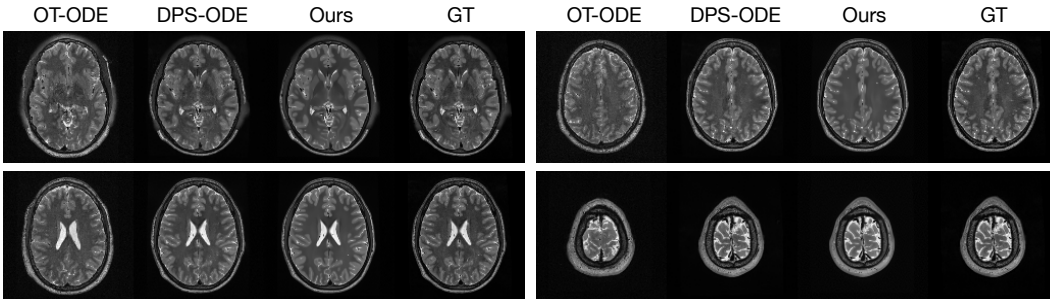


Figure 3: Qualitative comparison results on compressed sensing. Our method produces more faithful reconstructions with fewer artifacts, ensuring higher accuracy and clarity in the details.

All experiments incorporate Gaussian measurement noise with $\sigma_y = 0.01$. We address the following linear inverse problems: (1) $4\times$ super-resolution using bicubic downsampling, (2) inpainting with a random mask covering 70% of missing values, (3) Gaussian deblurring with a 61×61 kernel and a standard deviation of 3.0, and (4) box inpainting with a centered 128×128 mask.

We present the quantitative and qualitative results of all the methods in Tab. 1 and Fig. 2, respectively. In Tab. 1, our method surpasses all other baselines across all tasks. For more challenging tasks such as Gaussian deblurring and box inpainting, our method significantly outperforms others in terms of SSIM. Based on the MAP framework, as shown in Fig. 2, our method prefers more faithful and artifact-free reconstructions, whereas others trade off for perceptual quality. We note that there is an unavoidable tradeoff between perceptual quality and restoration faithfulness [3]. Overall, our method presents a higher degree of refinement. The comparison between ours and ours (w/o prior) indicates the effectiveness of the local prior term in enhancing the accuracy of the reconstructions, as evidenced by the increases in both PSNR and SSIM.

4.2 Medical application

HCP T2w dataset We utilize images from the publicly available Human Connectome Project (HCP) [50] T2-weighted (T2w) images dataset for the task of compressed sensing, which contains brain images from 47 patients. The HCP dataset includes cross-sectional images of the brain taken at different levels and angles.

Compressed sensing We train a flow-based model from scratch on 10,000 randomly sampled images, utilizing the *ncsnpp* architecture [48] with minor adaptations for grayscale images. We employ compression rates $\nu \in \{1/2, 1/4, 1/10\}$, meaning $m = \nu n$. The measurement operator is given by a subsampled Fourier matrix, whose sign patterns are randomly selected. We evaluate our reconstruction algorithm’s performance on 200 randomly sampled test images.

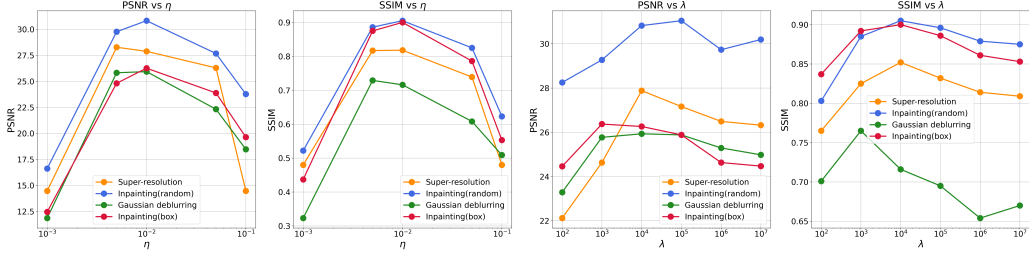


Figure 4: Ablation results of step size η and guidance weight λ . The choice of hyperparameters for our algorithm is fairly consistent across all tasks. We choose $\eta = 10^{-2}$ for all experiments on CelebA-HQ. For λ , we choose $\lambda = 10^3$ for Gaussian deblurring and $\lambda = 10^4$ for the other tasks.

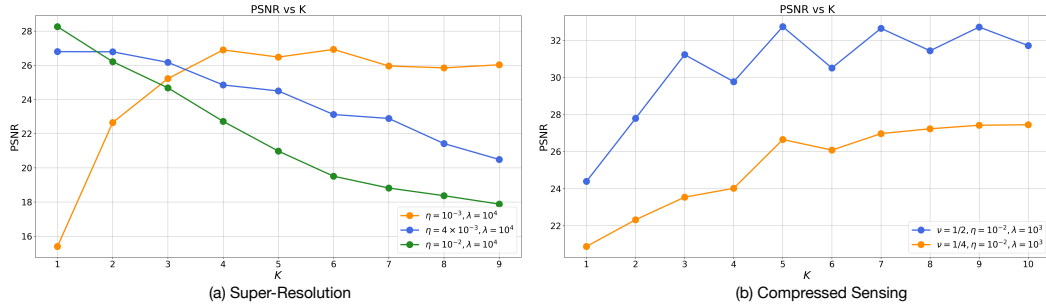


Figure 5: Ablation results of iteration number K on different tasks. For super-resolution and the other three tasks, $K = 1$ is sufficient to achieve the best performance with the optimal step size η and guidance weight λ . However, for compressed sensing, it is necessary to increase K to obtain the best performance. We hypothesize that this is due to the increased complexity of the compressed sensing operator, which requires more iteration steps to ensure the correct optimization direction.

We present the quantitative and qualitative results of compressed sensing in Tab. 2 and Fig. 3, respectively. In addition to flow-based methods, we include results for two classical recovery algorithms, Wavelet [11, 32] and TV [22] priors. As shown in Tab. 2, our method outperforms the classical recovery algorithms and other flow-based baselines across varying compression rates ν , demonstrating our method’s capability to handle challenging scenarios and the advantages of utilizing modern generative models as priors. In Fig. 3, our method produces reconstructions that are more faithful to the original images, with fewer artifacts, leading to higher accuracy and clearer details.

4.3 Ablation studies

We use the Adam optimizer [26] for our optimization steps due to its effectiveness in neural network computations. For all tasks, we utilize $N = 100$ steps.

Step size η and Guidance weight λ The use of the Adam optimizer ensures that the choice of hyperparameters, particularly the step size η and the guidance weight λ , remains consistent across various tasks, as illustrated in Fig. 4. Specifically, a step size of $\eta = 10^{-2}$ is optimal for Inpainting (random), Inpainting (box), and Super-resolution in terms of SSIM. For PSNR, Gaussian deblurring also achieves optimal performance at $\eta = 10^{-2}$. Consequently, we employ $\eta = 10^{-2}$ for all tasks. Based on the results shown in the right two subfigures of Fig. 4, we select $\lambda = 10^3$ for Gaussian deblurring and $\lambda = 10^4$ for the other tasks. This consistency extends to the compressed sensing experiments, where we set $\lambda = 10^3$ and $\eta = 10^{-2}$ for all experiments involving medical images.

Iteration number K We present ablation results of the iteration number K on different tasks in Fig. 5. We focus on the behavior of K in super-resolution and compressed sensing, as it performs similarly

to super-resolution in the other three tasks. With the optimal choice of η and λ in super-resolution, i.e., $\eta = 10^{-2}$ and $\lambda = 10^3$, $K = 1$ provides superior performance on CelebA-HQ. A decreased step size, e.g., $\eta = 10^{-3}$, can help performance as K increases, but it fails to exceed the performance achieved with the optimal parameters at $K = 1$. However, for compressed sensing, it is necessary to increase K to achieve the best performance. Consequently, we set $K = 10$ for all compressed sensing experiments. We hypothesize that the complexity of the compressed sensing operator directly determines the number of iterations required for optimal performance.

5 Conclusion

In this work, we have introduced a novel iterative algorithm to incorporate flow priors to solve linear inverse problems. By addressing the computational challenges associated with the slow log-likelihood calculations inherent in flow matching models, our approach leverages the decomposition of the MAP objective into multiple "local MAP" objectives. This decomposition, combined with the application of Tweedie's formula, enables effective sequential optimization through gradient steps. Our method has been rigorously validated on both natural and scientific images across various linear inverse problems, including super-resolution, deblurring, inpainting, and compressed sensing. The empirical results indicate that our algorithm consistently outperforms existing techniques based on flow matching, highlighting its potential as a powerful tool for high-resolution image synthesis and related downstream tasks.

6 Limitations and Future Work

While our algorithm has demonstrated promising results, there are certain limitations that suggest avenues for future research. First, our theoretical framework, built on optimal transport interpolation paths, is currently limited and cannot be applied to solve the general interpolation between Gaussian and data distributions. Additionally, in order to broaden the applicability of flow priors for inverse problems, it is important to generalize our approach to handle nonlinear forward models. Moreover, the algorithm currently lacks the capability to quantify the uncertainty of the generated images, an aspect crucial for many scientific applications. It would be interesting to consider approaches to post-process our solutions to understand the uncertainty inherent in our reconstruction. These limitations highlight important directions for future work to enhance the robustness and applicability of our method.

Acknowledgements

The work was partially supported by NSF DMS-2015577, NSF DMS-2415226, and a gift fund from Amazon. We thank anonymous reviewers for their feedback and suggestions, which helped improve the quality of the paper.

References

- [1] Muhammad Asim, Max Daniels, Oscar Leong, Ali Ahmed, and Paul Hand. Invertible generative models for inverse problems: mitigating representation error and dataset bias. *Proceedings of the 37th International Conference on Machine Learning*, 2020.
- [2] Heli Ben-Hamu, Omri Puny, Itai Gat, Brian Karrer, Uriel Singer, and Yaron Lipman. D-flow: Differentiating through flows for controlled generation. In *Forty-first International Conference on Machine Learning*, 2024.
- [3] Yochai Blau and Tomer Michaeli. The perception-distortion tradeoff. In *Proceedings of the IEEE conference on computer vision and pattern recognition*, pages 6228–6237, 2018.
- [4] Ashish Bora, Ajil Jalal, Eric Price, and Alexandros Dimakis. Compressed sensing using generative models. *International Conference on Machine Learning*, 2017.
- [5] Steve Brooks, Andrew Gelman, Galin Jones, and Xiao-Li Meng. *Handbook of markov chain monte carlo*. CRC press, 2011.
- [6] Martin Burger and Felix Lucka. Maximum a posteriori estimates in linear inverse problems with log-concave priors are proper bayes estimators. *Inverse Problems*, 30(11):114004, 2014.
- [7] Thorsten M Buzug. Computed tomography. In *Springer handbook of medical technology*, pages 311–342. Springer, 2011.
- [8] Yingshan Chang, Yasi Zhang, Zhiyuan Fang, Yingnian Wu, Yonatan Bisk, and Feng Gao. Skews in the phenomenon space hinder generalization in text-to-image generation, 2024.
- [9] Ricky T. Q. Chen, Yulia Rubanova, Jesse Bettencourt, and David K Duvenaud. Neural ordinary differential equations. In S. Bengio, H. Wallach, H. Larochelle, K. Grauman, N. Cesa-Bianchi, and R. Garnett, editors, *Advances in Neural Information Processing Systems*, volume 31. Curran Associates, Inc., 2018.
- [10] Hyungjin Chung, Jeongsol Kim, Michael T Mccann, Marc L Klasky, and Jong Chul Ye. Diffusion posterior sampling for general noisy inverse problems. In *The Eleventh International Conference on Learning Representations, ICLR 2023*. The International Conference on Learning Representations, 2023.
- [11] David L Donoho. Compressed sensing. *IEEE Transactions on information theory*, 52(4):1289–1306, 2006.
- [12] Bradley Efron. Tweedie’s formula and selection bias. *Journal of the American Statistical Association*, 106(496):1602–1614, 2011.
- [13] Patrick Esser, Sumith Kulal, Andreas Blattmann, Rahim Entezari, Jonas Müller, Harry Saini, Yam Levi, Dominik Lorenz, Axel Sauer, Frederic Boesel, et al. Scaling rectified flow transformers for high-resolution image synthesis. *arXiv preprint arXiv:2403.03206*, 2024.
- [14] Zhenghan Fang, Sam Buchanan, and Jeremias Sulam. What’s in a prior? learned proximal networks for inverse problems. In *International Conference on Learning Representations*, 2024.
- [15] Berthy Feng and Katherine Bouman. Variational bayesian imaging with an efficient surrogate score-based prior. *Transactions on Machine Learning Research*, 2024.
- [16] Berthy T Feng, Jamie Smith, Michael Rubinstein, Huiwen Chang, Katherine L Bouman, and William T Freeman. Score-based diffusion models as principled priors for inverse imaging. In *International Conference on Computer Vision (ICCV)*. IEEE, 2023.

- [17] Ian Goodfellow, Jean Pouget-Abadie, Mehdi Mirza, Bing Xu, David Warde-Farley, Sherjil Ozair, Aaron Courville, and Yoshua Bengio. Generative adversarial networks. *Communications of the ACM*, 63(11):139–144, 2020.
- [18] Will Grathwohl, Ricky T. Q. Chen, Jesse Bettencourt, Ilya Sutskever, and David Duvenaud. Ffjord: Free-form continuous dynamics for scalable reversible generative models. In *International Conference on Learning Representations*, 2019.
- [19] Tapio Helin and Martin Burger. Maximum a posteriori probability estimates in infinite-dimensional bayesian inverse problems. *Inverse Problems*, 31(8):085009, 2015.
- [20] Jonathan Ho, Ajay Jain, and Pieter Abbeel. Denoising diffusion probabilistic models. *Advances in neural information processing systems*, 33:6840–6851, 2020.
- [21] Michael F Hutchinson. A stochastic estimator of the trace of the influence matrix for laplacian smoothing splines. *Communications in Statistics-Simulation and Computation*, 18(3):1059–1076, 1989.
- [22] Leonid I. Rudin, Stanley Osher, and Emad Fatemi. Nonlinear total variation based noise removal algorithms. *Physica D: Nonlinear Phenomena*, 60:259–268, 1992.
- [23] Peter A Jansson. *Deconvolution of images and spectra*. Courier Corporation, 2014.
- [24] Tero Karras, Timo Aila, Samuli Laine, and Jaakko Lehtinen. Progressive growing of gans for improved quality, stability, and variation. *arXiv preprint arXiv:1710.10196*, 2017.
- [25] Diederik Kingma and Ruiqi Gao. Understanding diffusion objectives as the elbo with simple data augmentation. In A. Oh, T. Naumann, A. Globerson, K. Saenko, M. Hardt, and S. Levine, editors, *Advances in Neural Information Processing Systems*, volume 36, pages 65484–65516. Curran Associates, Inc., 2023.
- [26] Diederik P Kingma and Jimmy Ba. Adam: A method for stochastic optimization. *arXiv preprint arXiv:1412.6980*, 2014.
- [27] Diederik P Kingma and Max Welling. Auto-encoding variational bayes. *arXiv preprint arXiv:1312.6114*, 2013.
- [28] Yaron Lipman, Ricky TQ Chen, Heli Ben-Hamu, Maximilian Nickel, and Matthew Le. Flow matching for generative modeling. In *The Eleventh International Conference on Learning Representations*, 2022.
- [29] Xingchao Liu, Chengyue Gong, et al. Flow straight and fast: Learning to generate and transfer data with rectified flow. In *The Eleventh International Conference on Learning Representations*, 2022.
- [30] Xingchao Liu, Xiwen Zhang, Jianzhu Ma, Jian Peng, and Qiang Liu. InstafLOW: One step is enough for high-quality diffusion-based text-to-image generation. In *International Conference on Learning Representations*, 2024.
- [31] Ziwei Liu, Ping Luo, Xiaogang Wang, and Xiaoou Tang. Deep learning face attributes in the wild. In *Proceedings of the IEEE international conference on computer vision*, pages 3730–3738, 2015.
- [32] Michael Lustig, David L. Donoho, Juan M. Santos, and John M. Pauly. Compressed sensing mri. *IEEE Signal Processing Magazine*, 25(2):72–82, 2008.
- [33] Morteza Mardani, Jiaming Song, Jan Kautz, and Arash Vahdat. A variational perspective on solving inverse problems with diffusion models. In *The Twelfth International Conference on Learning Representations*, 2024.
- [34] Sachit Menon, Alex Damian, McCourt Hu, Nikhil Ravi, and Cynthia Rudin. Pulse: Self-supervised photo upsampling via latent space exploration of generative models. In *The IEEE Conference on Computer Vision and Pattern Recognition (CVPR)*, June 2020.
- [35] Guust Nolet. A breviary of seismic tomography. *A breviary of seismic tomography*, 2008.

- [36] Gregory Ongie, Ajil Jalal, Christopher A. Metzler, Richard G. Baraniuk, Alexandros G. Dimakis, and Rebecca Willett. Deep learning techniques for inverse problems in imaging. *IEEE Journal on Selected Areas in Information Theory*, 1(1):39–56, 2020.
- [37] Ashwini Pokle, Matthew J Muckley, Ricky TQ Chen, and Brian Karrer. Training-free linear image inversion via flows. *arXiv preprint arXiv:2310.04432*, 2023.
- [38] Saiprasad Ravishankar, Jong Chul Ye, and Jeffrey A Fessler. Image reconstruction: From sparsity to data-adaptive methods and machine learning. *Proceedings of the IEEE*, 108(1):86–109, 2019.
- [39] Nicholas Rawlinson, Andreas Fichtner, Malcolm Sambridge, and Mallory K Young. Seismic tomography and the assessment of uncertainty. *Advances in geophysics*, 55:1–76, 2014.
- [40] Danilo Rezende and Shakir Mohamed. Variational inference with normalizing flows. In *International conference on machine learning*, pages 1530–1538. PMLR, 2015.
- [41] François Roddier. Interferometric imaging in optical astronomy. *Physics Reports*, 170(2):97–166, 1988.
- [42] Olaf Ronneberger, Philipp Fischer, and Thomas Brox. U-net: Convolutional networks for biomedical image segmentation. In *Medical image computing and computer-assisted intervention—MICCAI 2015: 18th international conference, Munich, Germany, October 5-9, 2015, proceedings, part III 18*, pages 234–241. Springer, 2015.
- [43] Litu Rout, Negin Raof, Giannis Daras, Constantine Caramanis, Alex Dimakis, and Sanjay Shakkottai. Solving linear inverse problems provably via posterior sampling with latent diffusion models. *Advances in Neural Information Processing Systems*, 36, 2024.
- [44] John Skilling. The eigenvalues of mega-dimensional matrices. *Maximum Entropy and Bayesian Methods: Cambridge, England, 1988*, pages 455–466, 1989.
- [45] Jascha Sohl-Dickstein, Eric Weiss, Niru Maheswaranathan, and Surya Ganguli. Deep unsupervised learning using nonequilibrium thermodynamics. In *International conference on machine learning*, pages 2256–2265. PMLR, 2015.
- [46] Jiaming Song, Arash Vahdat, Morteza Mardani, and Jan Kautz. Pseudoinverse-guided diffusion models for inverse problems. In *International Conference on Learning Representations*, 2023.
- [47] Yang Song, Conor Durkan, Iain Murray, and Stefano Ermon. Maximum likelihood training of score-based diffusion models. *Advances in neural information processing systems*, 34:1415–1428, 2021.
- [48] Yang Song, Jascha Sohl-Dickstein, Diederik P Kingma, Abhishek Kumar, Stefano Ermon, and Ben Poole. Score-based generative modeling through stochastic differential equations. *arXiv preprint arXiv:2011.13456*, 2020.
- [49] Paul Suetens. *Fundamentals of medical imaging*. Cambridge university press, 2017.
- [50] David C Van Essen, Stephen M Smith, Deanna M Barch, Timothy EJ Behrens, Essa Yacoub, Kamil Ugurbil, Wu-Minn HCP Consortium, et al. The wu-minn human connectome project: an overview. *Neuroimage*, 80:62–79, 2013.
- [51] Ashish Vaswani, Noam Shazeer, Niki Parmar, Jakob Uszkoreit, Llion Jones, Aidan N Gomez, Łukasz Kaiser, and Illia Polosukhin. Attention is all you need. *Advances in neural information processing systems*, 30, 2017.
- [52] Marinus T Vlaardingerbroek and Jacques A Boer. *Magnetic resonance imaging: theory and practice*. Springer Science & Business Media, 2013.
- [53] Zhou Wang, A.C. Bovik, H.R. Sheikh, and E.P. Simoncelli. Image quality assessment: from error visibility to structural similarity. *IEEE Transactions on Image Processing*, 13(4):600–612, 2004.

- [54] Jay Whang, Erik M. Lindgren, and Alexandros G. Dimakis. Composing normalizing flows for inverse problems. *Proceedings of the 38th International Conference on Machine Learning*, 2021.
- [55] Jianwen Xie, Yang Lu, Song-Chun Zhu, and Yingnian Wu. A theory of generative convnet. In Maria Florina Balcan and Kilian Q. Weinberger, editors, *Proceedings of The 33rd International Conference on Machine Learning*, volume 48 of *Proceedings of Machine Learning Research*, pages 2635–2644, New York, New York, USA, 20–22 Jun 2016. PMLR.
- [56] Hanshu Yan, Xingchao Liu, Jiachun Pan, Jun Hao Liew, Qiang Liu, and Jiashi Feng. Perflow: Piecewise rectified flow as universal plug-and-play accelerator. *arXiv preprint arXiv:2405.07510*, 2024.
- [57] Peiyu Yu, Dinghuai Zhang, Hengzhi He, Xiaojian Ma, Ruiyao Miao, Yifan Lu, Yasi Zhang, Deqian Kong, Ruiqi Gao, Jianwen Xie, Guang Cheng, and Ying Nian Wu. Latent energy-based odyssey: Black-box optimization via expanded exploration in the energy-based latent space, 2024.
- [58] Yasi Zhang, Peiyu Yu, and Ying Nian Wu. Object-conditioned energy-based attention map alignment in text-to-image diffusion models. *arXiv preprint arXiv:2404.07389*, 2024.
- [59] Yaxuan Zhu, Zehao Dou, Haoxin Zheng, Yasi Zhang, Ying Nian Wu, and Ruiqi Gao. Think twice before you act: Improving inverse problem solving with mcmc. *arXiv preprint arXiv:2409.08551*, 2024.

Appendix

A Proof

Before we dive into the proof, we provide the following three lemmas.

Lemma 1. Consider a vector-valued function $f : [0, 1] \rightarrow \mathbb{R}^n$. Then for any $t \in [0, 1]$, we have that

$$\left\| \int_0^t f(s) ds \right\|^2 \leq \int_0^t \|f(s)\|^2 ds.$$

Proof. For each $s \in [0, 1]$, let $f_i(s) \in \mathbb{R}$ denote the i -th component of $f(s)$. Recall Jensen's inequality: for any convex function $g : \mathbb{R} \rightarrow \mathbb{R}$ and integrable function $h : [0, 1] \rightarrow \mathbb{R}$, we have

$$g\left(\int_a^b h(t) dt\right) \leq \int_a^b g(h(t)) dt.$$

Using convexity of the function $t \mapsto t^2$ and applying Jensen's inequality, we see that

$$\begin{aligned} \left\| \int_0^t f(s) ds \right\|^2 &= \sum_{i=1}^n \left(\int_0^t f_i(s) ds \right)^2 \\ &\leq \sum_{i=1}^n \int_0^t f_i(s)^2 ds \\ &= \int_0^t \sum_{i=1}^n f_i(s)^2 ds \\ &= \int_0^t \|f(s)\|^2 ds. \end{aligned}$$

□

Lemma 2 (Tweedie's Formula [12]). If $\mu \sim g(\cdot)$, $z|\mu \sim \mathcal{N}(\alpha\mu, \sigma^2 I)$, and therefore $z \sim f(\cdot)$, we have

$$\mathbb{E}[\mu|z] = \frac{1}{\alpha} [z + \sigma^2 \nabla_z \log f(z)]. \quad (12)$$

Lemma 3. Suppose $y = \mathcal{A}(x_*) + \epsilon$ where $x_* = x_1(x_0)$ with x_0 being the solution to Eq. (9), $\mathcal{A} : \mathbb{R}^n \rightarrow \mathbb{R}^m$ is linear, $\epsilon \sim \mathcal{N}(0, \sigma_y^2 I)$, and x_t exactly follows the path $x_t = \alpha_t x + \beta_t x_0$ for any time $t \in [0, 1]$. Then we have

$$p(y_t|x_t) = \mathcal{N}(\mathcal{A}x_t, \alpha_t^2 \sigma_y^2 I), \quad (13)$$

and hence

$$\log p(y|x(x_0)) = \log p(y_t|x_t) + \frac{m}{2} \log(\alpha_t^2), \forall t. \quad (14)$$

Proof. Recall that the generated auxiliary path $y_t = \alpha_t y + \beta_t \mathcal{A}x_0$. By assumption, we have $\mathcal{A}(x_t) = \mathcal{A}(\alpha_t x + \beta_t x_0) = \alpha_t \mathcal{A}(x(x_0)) + \beta_t \mathcal{A}x_0$. By subtracting these two equations, we have

$$y_t - \mathcal{A}(x_t) = \alpha_t (y - \mathcal{A}(x(x_0))). \quad (15)$$

As $y|x(x_0) \sim \mathcal{N}(\mathcal{A}x, \sigma_y^2 I)$, we have $y_t|x_t \sim \mathcal{N}(\mathcal{A}x_t, \alpha_t^2 \sigma_y^2 I)$. The proof for Eq. (13) is done. Next, we examine the log probability as follows:

$$\log p(y_t|x_t) = -\frac{\|y_t - \mathcal{A}x_t\|^2}{2\alpha_t^2 \sigma_y^2} - \frac{m}{2} \log(2\pi \alpha_t^2 \sigma_y^2) \quad (16)$$

$$= -\frac{\|\alpha_t (y - \mathcal{A}(x(x_0)))\|^2}{2\alpha_t^2 \sigma_y^2} - \frac{m}{2} \log(2\pi \alpha_t^2 \sigma_y^2) \quad (17)$$

$$= -\frac{\|y - \mathcal{A}(x(x_0))\|^2}{2\sigma_y^2} - \frac{m}{2} \log(2\pi \sigma_y^2) - \frac{m}{2} \log(\alpha_t^2) \quad (18)$$

$$:= \log p(y|x(x_0)) - \frac{m}{2} \log(\alpha_t^2). \quad (19)$$

□

A.1 Proof of Proposition 1

Trained by the objective defined in Eq. (5), the optimal velocity field would be

$$v_\theta(x_t, t) = \mathbb{E}(\dot{\alpha}_t x_1 + \dot{\beta}_t x_0 | x_t) \quad (20)$$

$$= \mathbb{E}\left(\dot{\alpha}_t x_1 + \dot{\beta}_t \frac{x_t - \alpha_t x}{\beta_t} \middle| x_t\right) \quad \# \text{ Given } x_t, x_0 = \frac{x_t - \alpha_t x}{\beta_t} \quad (21)$$

$$= (\dot{\alpha}_t - \dot{\beta}_t \frac{\alpha_t}{\beta_t}) \mathbb{E}(x_1 | x_t) + \frac{\dot{\beta}_t}{\beta_t} x_t \quad (22)$$

$$= (\dot{\alpha}_t - \dot{\beta}_t \frac{\alpha_t}{\beta_t}) \left[\frac{1}{\alpha_t} (x_t + \beta_t^2 \nabla_{x_t} \log p(x_t)) \right] + \frac{\dot{\beta}_t}{\beta_t} x_t. \quad \# \text{ Lemma 2 (Tweedie's Formula)} \quad (23)$$

By defining the signal-to-noise ratio as $\lambda_t = \alpha_t / \beta_t$ and rearranging the equation above, we get exactly Eq. (11) which we display again below:

$$\nabla_{x_t} \log p(x_t) = \frac{1}{\beta_t^2} \left[\left(\frac{d \log \lambda_t}{dt} \right)^{-1} \left(v_\theta(x_t, t) - \frac{d \log \beta_t}{dt} x_t \right) - x_t \right]. \quad (24)$$

When $\alpha_t = t, \beta_t = 1 - t$, the equation above becomes

$$\nabla_{x_t} \log p(x_t) = \frac{1}{1-t} (-x_t + t v_\theta(x_t, t)). \quad (25)$$

A.2 Proof of Theorem 1

Before we dive into the proof, we first point out $\lim_{\Delta t \rightarrow 0} \sum_{i=1}^N \gamma_i = 1$. Define the timestep $t = (i-1)\Delta t$. Conversely, $i = 1 + t/\Delta t$ is a function of t . In this sense, we define the i -th step Riemannian discretization of the integral $-\int_0^1 \text{tr} \left(\frac{\partial v_\theta(x_t, t)}{\partial x} \right) dt$ as $\Delta p_i = -\text{tr} \left(\frac{\partial v_\theta(x_t, t)}{\partial x} \right) \Delta t$.

We first decompose the global MAP objective as follows:

$$\log p(x(x_0) | y) = \log p(x_0) - \int_0^1 \text{tr} \left(\frac{\partial v_\theta(x_t, t)}{\partial x} \right) dt + \log p(y | x(x_0)) - \log p(y) \quad (26)$$

$$= \lim_{\Delta t \rightarrow 0} \sum_{i=1}^N \gamma_i \log p(x_0) + \lim_{\Delta t \rightarrow 0} \sum_{i=1}^N \Delta p_i \quad (27)$$

$$+ \lim_{\Delta t \rightarrow 0} \sum_{i=1}^N \gamma_i [\log p(y_{i\Delta t} | x_{i\Delta t}) + c_i] - \log p(y), \quad (28)$$

where the decomposition of the second term utilizes the property of the discretization of Riemann integral, and that of the third term utilizes the result in Lemma 3 and thus $c_i = \frac{m}{2} \log(\alpha_{i\Delta t}^2)$. By the property of limits, i.e. $\lim_{\Delta t \rightarrow 0} (\sum_{i=1}^N \gamma_i) (\sum_{i=1}^N \Delta p_i) = \lim_{\Delta t \rightarrow 0} (\sum_{i=1}^N \gamma_i) \lim_{\Delta t \rightarrow 0} (\sum_{i=1}^N \Delta p_i) = \lim_{\Delta t \rightarrow 0} \sum_{i=1}^N \Delta p_i$, we can further decompose the second term in Eq. (28) into $\lim_{\Delta t \rightarrow 0} (\sum_{i=1}^N \gamma_i) (\sum_{i=1}^N \Delta p_i)$.

By extracting the limit out in Eq. (28), the equation becomes

$$\begin{aligned} & \lim_{\Delta t \rightarrow 0} \left\{ \gamma_1 [\log p(x_0) + \Delta p_1 + \log p(y_{\Delta t} | x_{\Delta t}) + c_1] \right. \\ & \quad + \gamma_2 [\log p(x_0) + \Delta p_1 + \Delta p_2 + \log p(y_{2\Delta t} | x_{2\Delta t}) + c_2] \\ & \quad + \dots \\ & \quad + \gamma_N [\log p(x_0) + \Delta p_1 + \Delta p_2 + \dots + \Delta p_N + \log p(y_{N\Delta t} | x_{N\Delta t}) + c_N] \\ & \quad \left. + [\gamma_1 \Delta p_2 + (\gamma_1 + \gamma_2) \Delta p_3 + \dots + (\gamma_1 + \gamma_2 + \dots + \gamma_{N-1}) \Delta p_N] - \log p(y) \right\} \quad (29) \end{aligned}$$

$$:= \lim_{\Delta t \rightarrow 0} \left[\sum_{i=1}^N \gamma_i \tilde{\mathcal{J}}_i + \sum_{j=2}^N \left(\sum_{i=1}^{j-1} \gamma_i \right) \Delta p_j + \sum_{i=1}^N \gamma_i c_i - \log p(y) \right], \quad (30)$$

where $\tilde{\mathcal{J}}_i := \log p(x_0) + \sum_{j=1}^i \Delta p_j + \log p(y_{i\Delta t} | x_{i\Delta t})$. We further define the $c(N) = \sum_{i=1}^N \gamma_i c_i - \log p(y)$.

Recall that $\hat{\mathcal{J}}_i = \log p(x_{(i-1)\Delta t}) - \text{tr} \left(\frac{\partial v_\theta(x_{(i-1)\Delta t}, (i-1)\Delta t)}{\partial x} \right) \Delta t + \log p(y_{i\Delta t} | x_{i\Delta t})$. By triangle inequality, we have

$$\left| \log p(x(x_0)|y) - \sum_{i=1}^N \gamma_i \hat{\mathcal{J}}_i - c(N) \right| \quad (31)$$

$$\leq \left| \log p(x(x_0)|y) - \sum_{i=1}^N \gamma_i \tilde{\mathcal{J}}_i - c(N) \right| + \left| \sum_{i=1}^N \gamma_i \hat{\mathcal{J}}_i - \sum_{i=1}^N \gamma_i \tilde{\mathcal{J}}_i \right|. \quad (32)$$

Taking the limit on both sides, we have

$$\lim_{\Delta t \rightarrow 0} \left| \log p(x(x_0)|y) - \sum_{i=1}^N \gamma_i \hat{\mathcal{J}}_i - c(N) \right| \quad (33)$$

$$\leq \lim_{\Delta t \rightarrow 0} \left| \log p(x(x_0)|y) - \sum_{i=1}^N \gamma_i \tilde{\mathcal{J}}_i - c(N) \right| + \lim_{\Delta t \rightarrow 0} \left| \sum_{i=1}^N \gamma_i \hat{\mathcal{J}}_i - \sum_{i=1}^N \gamma_i \tilde{\mathcal{J}}_i \right|. \quad (34)$$

In the following, we analyze the two terms on the right-hand side one by one. For the first term: as $|\cdot| : \mathbb{R} \rightarrow \mathbb{R}$ is a continuous function, the first term on the right-hand side is equal to

$$\left| \log p(x(x_0)|y) - \lim_{\Delta t \rightarrow 0} \sum_{i=1}^N \gamma_i \tilde{\mathcal{J}}_i - c(N) \right| \quad (35)$$

$$= \left| \lim_{\Delta t \rightarrow 0} \sum_{j=2}^N \left(\sum_{i=1}^{j-1} \gamma_i \right) \Delta p_j \right| \quad (36)$$

$$= \left| \lim_{\Delta t \rightarrow 0} \sum_{j=2}^N \left(\frac{1}{2^{N-j+1}} - \frac{1}{2^N} \right) \Delta p_j \right| \quad (37)$$

$$\leq \left| \lim_{\Delta t \rightarrow 0} \sum_{j=2}^N \left(\frac{1}{2^{N-j+1}} \right) \Delta p_j \right| + \left| \lim_{\Delta t \rightarrow 0} \sum_{j=2}^N \left(\frac{1}{2^N} \right) \Delta p_j \right|, \quad (38)$$

where the first equation is derived by subtracting the first term in Eq. (30) from Eq. (26). As the velocity field $v_\theta : \mathbb{R}^n \times \mathbb{R} \rightarrow \mathbb{R}^n$ satisfies $\sup_{z \in \mathbb{R}^n, s \in [0,1]} |\text{tr} \frac{\partial}{\partial x} v_\theta(z, s)| \leq C_1$ for some universal constant C_1 , we have $|\Delta p_j| \leq C_1 \Delta t$. The first term in (38) would be

$$\left| \sum_{j=2}^N \left(\frac{1}{2^{N-j+1}} \right) \Delta p_j \right| \leq C_1 \Delta t \sum_{j=2}^N \left(\frac{1}{2^{N-j+1}} \right) \leq C_1 \Delta t = O(\Delta t). \quad (39)$$

Similarly, the second term in (38) would be

$$\left| \sum_{j=2}^n \left(\frac{1}{2^n} \right) \Delta p_j \right| \leq \sum_{j=2}^n \left(\frac{1}{2^n} \right) C_1 \Delta t = C_1 \left(\frac{N-1}{2^N} \right) \Delta t = O(\Delta t). \quad (40)$$

Combining the results in Eq. (39) and Eq. (40), we get

$$\left| \log p(x(x_0)|y) - \lim_{\Delta t \rightarrow 0} \sum_{i=1}^N \gamma_i \tilde{\mathcal{J}}_i - c(N) \right| = 0. \quad (41)$$

For the second term: Intuitively, the error between the integral and the Riemannian discretization goes to 0 as Δt tends to 0. Rigorously,

$$\lim_{\Delta t \rightarrow 0} \left| \sum_{i=1}^N \gamma_i \hat{\mathcal{J}}_i - \sum_{i=1}^N \gamma_i \tilde{\mathcal{J}}_i \right| = \lim_{\Delta t \rightarrow 0} \left| \sum_{i=1}^N \gamma_i (\hat{\mathcal{J}}_i - \tilde{\mathcal{J}}_i) \right| \quad (42)$$

$$= \lim_{\Delta t \rightarrow 0} \left| \sum_{i=1}^N \gamma_i \left(\int_0^{t-\Delta t} \text{tr} \left(\frac{\partial v_\theta(x_s, s)}{\partial x} \right) ds - \sum_{j=1}^{i-1} \Delta p_j \right) \right| \quad (43)$$

$$\leq \lim_{\Delta t \rightarrow 0} \sum_{i=1}^N \gamma_i \left| \int_0^{t-\Delta t} \text{tr} \left(\frac{\partial v_\theta(x_s, s)}{\partial x} \right) ds - \sum_{j=1}^{i-1} \Delta p_j \right| = 0. \quad (44)$$

Combining the results of the first term and the second term, we get the proof of theorem 1 done.

B Compliance of Trajectory

To quantify our deviation from the assumption of having x_t exactly follow the interpolation path $\alpha_t x + \beta_t x_0$, we define the following: given a differentiable process $\{z_t\}$ and an interpolation path specified by $\alpha := \{\alpha_t\}$ and $\beta := \{\beta_t\}$, we define the trajectory's **compliance** $S_{\alpha, \beta}(\{z_t\})$ to the interpolation path as

$$S_{\alpha, \beta}(\{z_t\}) := \int_0^1 \mathbb{E}_{p(z_0), p(z_1)} \left[\|\dot{z}_t - (\dot{\alpha}_t z_1 + \dot{\beta}_t z_0)\|^2 \right] dt. \quad (45)$$

This generalizes the definition of straightness in [29] to general interpolation paths. We recover their definition by setting $\alpha_t = t$ and $\beta_t = 1 - t$. In certain cases, we have exact compliance with the predefined interpolation path. For example, when $\{z_t\}$ is generated by v_θ and $\alpha_t = t$ and $\beta_t = 1 - t$, note that $S_{\alpha, \beta}(\{z_t\}) = 0$ is equivalent to $v_\theta(z_t, t) = c$ where c is a constant, almost everywhere. This ensures that $z_1 = z_0 + c$. In this case, when generating the trajectory through an ODE solver with starting point x_0 and endpoint x_t , we have $x_t = \alpha_t x + \beta_t x_0, \forall t$. When $S_{\alpha, \beta}(\{z_t\})$ is not equal to 0, we show in Proposition 2 that we can bound the deviation of our trajectory from the interpolation path using this compliance measure. When specifying our result to Rectified Flow, we can obtain an additional bound showing that when using L -Rectified Flow, the deviation of the learned trajectory from the straight trajectory is bounded by $O(1/L)$.

Proposition 2. Consider a differentiable interpolation path specified by $\alpha := \{\alpha_t\}$ and $\beta := \{\beta_t\}$. Then the expected distance between the learned trajectory $z_t = z_0 + \int_0^t v_\theta(z_s, s) ds$ and the predefined trajectory $\hat{z}_t = z_0 + \int_0^t (\dot{\alpha}_s z_1 + \dot{\beta}_s z_0) ds$ can be bounded as

$$\mathbb{E}_{p(z_0), p(z_1)} [\|\hat{z}_t - z_t\|^2] \leq S_{\alpha, \beta}(\{z_t\}). \quad (46)$$

If the differentiable process $\{z_t\}$ is specified by L -Rectified Flow and $\alpha_t = t$ and $\beta_t = 1 - t$ for all $t \in [0, 1]$, then we additionally have

$$\mathbb{E}_{p(z_0), p(z_1)} [\|\hat{z}_t - z_t\|^2] \leq O\left(\frac{1}{L}\right). \quad (47)$$

Proof. At time t , we are interested in the distance between a real trajectory $z_t = z_0 + \int_0^t v_\theta(z_s, s) ds$ and a preferred trajectory $\hat{z}_t = z_0 + \int_0^t (\dot{\alpha}_s z_1 - \dot{\beta}_s z_0) ds$. Using the result in Lemma 1, the distance can be bounded by

$$\|\hat{z}_t - z_t\|^2 = \left\| \int_0^t [v_\theta(z_s, s) - (\dot{\alpha}_s z_1 - \dot{\beta}_s z_0)] ds \right\|^2 \quad (48)$$

$$\leq \int_0^t \|v_\theta(z_s, s) - (\dot{\alpha}_s z_1 - \dot{\beta}_s z_0)\|^2 ds. \quad (49)$$

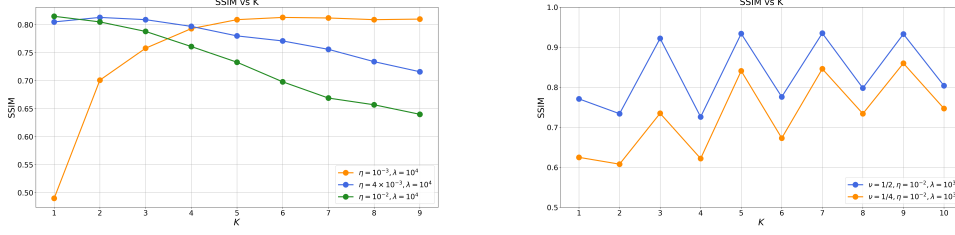


Figure 6: Ablation results of K in terms of SSIM on different tasks.

Therefore,

$$\mathbb{E}_{p(z_0), p(z_1)} \|\hat{z}_t - z_t\|^2 \leq \mathbb{E}_{p(z_0), p(z_1)} \left[\int_0^t \|v_\theta(z_s, s) - (\dot{\alpha}_s z_1 - \dot{\beta}_s z_0)\|^2 ds \right] \quad (50)$$

$$= \int_0^t \mathbb{E}_{p(z_0), p(z_1)} \|v_\theta(z_s, s) - (\dot{\alpha}_s z_1 - \dot{\beta}_s z_0)\|^2 ds \quad (51)$$

$$\leq \int_0^1 \mathbb{E}_{p(z_0), p(z_1)} \|v_\theta(z_s, s) - (\dot{\alpha}_s z_1 - \dot{\beta}_s z_0)\|^2 ds \quad (52)$$

$$:= S_{\alpha, \beta}(\{z\}). \quad (53)$$

If $\{z_t, t \in [0, 1]\}$ is a learned L -rectified flow, i.e. $\alpha_t = t$ and $\beta_t = 1 - t$ in this case, where L is the times of rectifying the flow, by Theorem 3.7 in [29], we have $S_{\alpha, \beta}(\{z\}) = O(1/L)$ and thus

$$\mathbb{E}_{p(z_0), p(z_1)} \|\hat{z}_t - z_t\|^2 = O(1/L). \quad (54)$$

□

Empirically, [30, 29] found $L = 2$ generates nearly straight trajectories for high-quality one-step generation. Hence, while this result gives us a simple upper bound, in practice the trajectories may comply more faithfully with the predefined interpolation path than this result suggests.

C Additional Results

C.1 Additional Ablations

Iteration steps K We provide additional ablation results of K in terms of SSIM in Fig. 6.

NFEs N We first refer to Fig. 1(c) for a preliminary ablation on N using a toy example. Next, we show PSNR and SSIM scores for varying N in the task of super-resolution. We find that $N = 100$ is the best trade-off between time and performance. The ablation results are shown in Fig. 7.

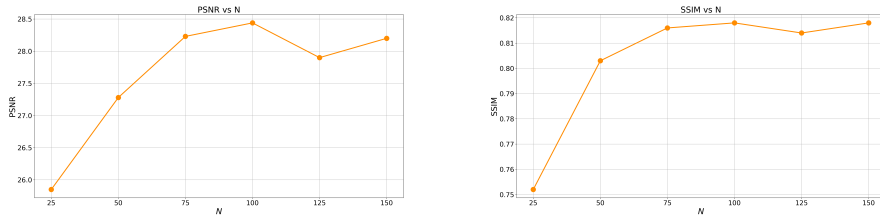


Figure 7: Ablation results of the NFEs N on the super-resolution task.

D Computational Efficiency

In Tab. 3, we present the computational efficiency comparison results. Note that OT-ODE is the slowest as it requires taking the inverse of a matrix $r_t^2 \mathcal{A} \mathcal{A}^T + \sigma_y^2 I$ each update time. Our

method requires taking the gradient over an estimated trace of the Jacobian matrix, which slows the computation.

Table 3: **Computational time comparison.** We compare the time required to recover 100 images for the super-resolution task on a single GPU.

| | DPS-ODE | OT-ODE | Ours (w/o prior) | Ours |
|---------|---------|--------|------------------|------|
| Time(h) | 0.36 | 4.10 | 0.83 | 2.72 |

E Implementation Details

Experiments were conducted on a Linux-based system with CUDA 12.2 equipped with 4 Nvidia R9000 GPUs, each of them has 48GB of memory.

Operators For all the experiments on the CelebA-HQ dataset, we use the operators from [10]. For all the experiments on compressed sensing, we use the operator *CompressedSensingOperator* defined in the official repository of [14]⁴,

Evaluation Metrics are implemented with different Python packages. PSNR is calculated using basic PyTorch operations, and SSIM is computed using the *pytorch_msssim* package.

E.1 Toy example

The workflow begins with using 1,000 FFHQ images at a resolution of 1024×1024 . These images are then downsampled to 16×16 using bicubic resizing. A Gaussian Mixture model is applied to fit the downsampled images, resulting in mean and covariance parameters. The mean values are transformed from the original range of $[0,1]$ to $[-1,1]$. Subsequently, 10,000 samples are generated from this distribution to facilitate training a score-based model resembling the architecture of CIFAR10 DDPM++. The training process involves 10,000 iterations, each with a batch size of 64, and utilizes the Adam optimizer [26] with a learning rate of $2e-4$ and a warmup phase lasting 100 steps. Notably, convergence is achieved within approximately 200 steps. Lastly, the estimated log-likelihood computation for a batch size of 128 takes around 4 minutes and 30 seconds. We show uncured samples generated from the trained models in Fig. 8.



Figure 8: Generated samples from the flow trained on 10,000 Gaussian samples.

⁴<https://github.com/Sulam-Group/learned-proximal-networks/tree/main>

E.2 Medical Application

In this setting, $\sigma_y = 0.001$. We use the *ncsnpp* architecture, training from scratch on 10k images for 100k iterations with a batch size of 50. We set the learning rate to 1×10^{-2} . Sudden convergence appeared during our training process. We use 2000 warmup steps. Uncured generated images are presented in Fig. 9.

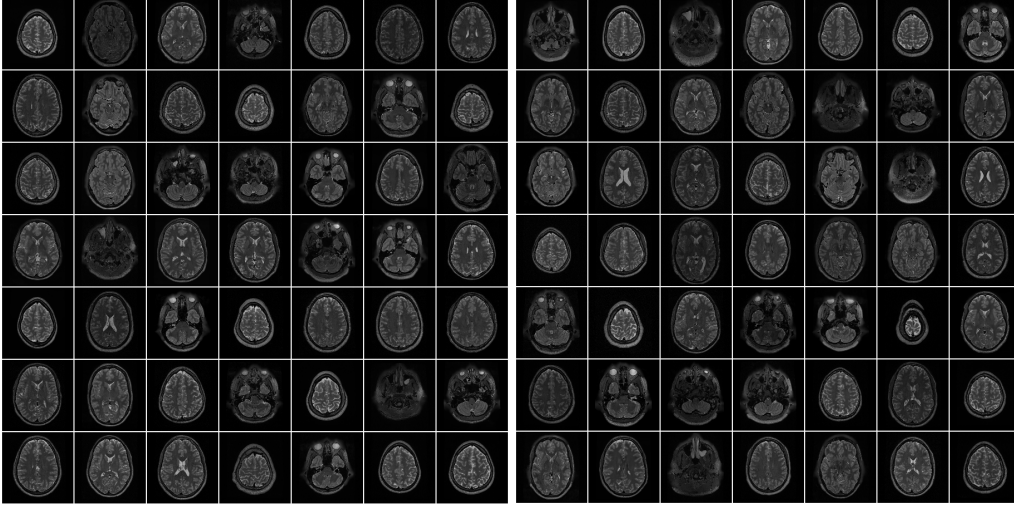


Figure 9: Generated samples from the flow trained on 10,000 HCP T2w images.

E.3 Implementation of Baselines

OT-ODE As OT-ODE [37] has not released their code and pretrained checkpoints. We reproduce their method with the same architecture as in [29]. We follow their setting and find initialization time t' has a great impact on the performance. We use the *y init* method in their paper. Specifically, the starting point is

$$x_{t'} = t'y + (1 - t')\epsilon, \epsilon \sim \mathcal{N}(0, I), \quad (55)$$

where t' is the init time. Note that in the super-resolution task we upscale y with bicubic first. We follow the guidance in the paper and show the ablation results in Fig. 10 and Fig. 11.

DPS-ODE We use the following formula to update for each step in the flow:

$$v(x_t, y) = v(x_t) + \zeta_t (-\nabla_{x_t} \|y - \mathcal{A}\hat{x}_1\|^2),$$

where ζ_t is the step size to tune. We refer to DPS for the method to choose ζ_t . We set $\zeta_t = \frac{\eta}{2\|y - \mathcal{A}\hat{x}_1(x_t)\|}$. We demonstrate the ablation of η for this baseline in Fig. 12 and Fig. 13. Note that there is a significant divergence in PSNR and SSIM for the task of inpainting (box). As we observe that artifacts are likely to appear when $\eta \geq 100$, we choose the optimal $\eta = 75$ for the best tradeoff.

RED-Diff and Π GDM We use the official repository⁵ from Nvidia to reproduce the results of RED-Diff and Π GDM with the pretrained CelebAHQ checkpoint using the architecture of the guided diffusion repository⁶ from OpenAI.

For RED-Diff, the optimization objective is $\min_{\mu} \|y - \mathcal{A}(\mu)\|^2 + \lambda(\text{sg}(\epsilon_{\theta}(x_t, t) - \epsilon))^T \mu$. Following the implementation of the original paper, we use Adam optimizer with 1,000 steps for all tasks. We choose learning rate $lr = 0.25$, $\lambda = 0.25$ for super-resolution, inpainting(random) and inpainting(box) and $lr = 0.5$, $\lambda = 0.25$ for deblurring as recommended by the paper.

⁵<https://github.com/NVlabs/RED-diff>

⁶<https://github.com/openai/guided-diffusion>

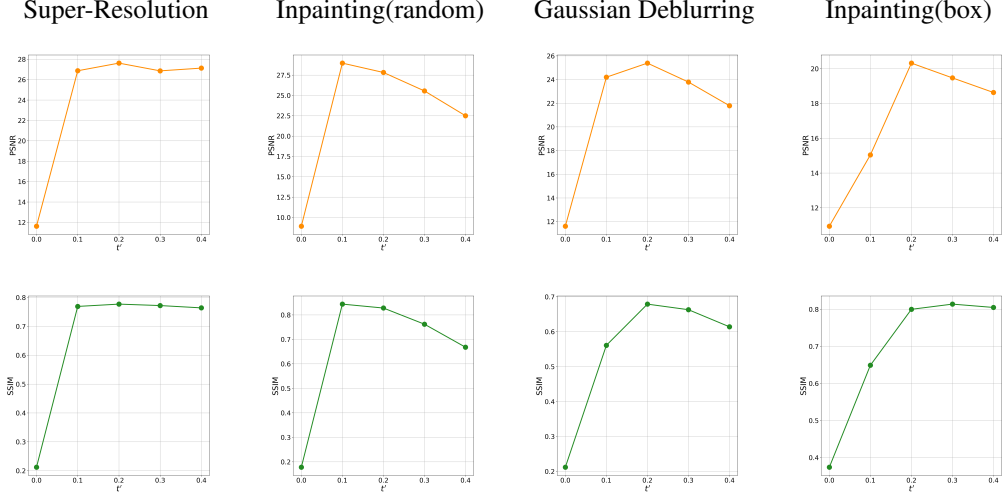


Figure 10: Hyperparameter t' selection results for OT-ODE on the CelebA-HQ dataset. We select $t' = 0.2, 0.1, 0.2, 0.2$ for super-resolution, inpainting(random), Gaussian deblurring, and inpainting(box), respectively.

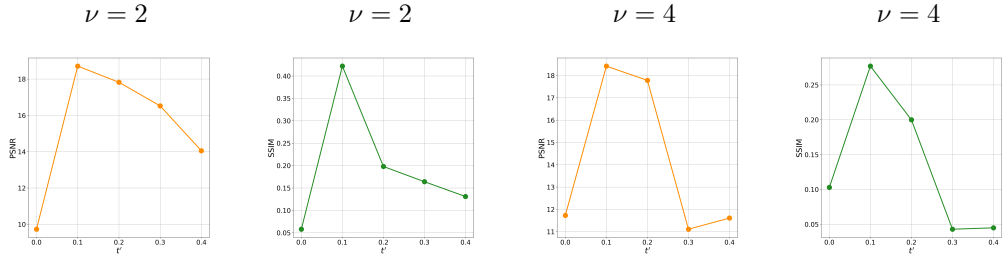


Figure 11: Hyperparameter t' selection results for OT-ODE on the HCP T2w dataset. We select $t' = 0.1$ for all the experiments.

For IIGDM, we follow the original paper and use 100 diffusion steps. Specifically, we use $\eta = 1.0$ which corresponds to the VE-SDE. Adaptive weights $r_t^2 = \frac{\sigma_{1-t}^2}{1+\sigma_t^2}$ are used if there is an improvement on metrics.

Wavelet and TV priors We use the pytorch package DeepInverse⁷ to implement Wavelet and TV priors. For both priors, we use the default Proximal Gradient Descent (PGD) algorithm and perform a grid search for regularization weight λ in the set $\{10^0, 10^{-1}, 10^{-2}, 10^{-3}, 10^{-4}\}$ and gradient stepsize η in $\{10^1, 10^0, 10^{-1}, 10^{-2}, 10^{-3}, 10^{-4}\}$. The maximum number of iteration is 3k, 5k, and 10k for compression rate $\nu = 1/2, 1/4$, and $1/10$, respectively. The stopping criterion is the residual norm $\frac{\|x_{t-1} - x_t\|}{\|x_{t-1}\|} \leq 1 \times 10^{-5}$ and the initialization of the algorithm is the backprojected reconstruction, i.e., the pseudoinverse of \mathcal{A} applied to the measurement y .

For the TV prior, the objective we aim to minimize is $\min_x \frac{1}{2} \|\mathcal{A}x - y\|_2^2 + \lambda \|x\|_{TV}$. We find that the optimal combination of hyperparameters is $\lambda = 0.01, \eta = 0.1$ for all the values of ν .

For the Wavelet prior, the objective we want to minimize is $\min_x \frac{1}{2} \|\mathcal{A}x - y\|_2^2 + \lambda \|\Psi x\|_1$. We use the default level of the wavelet transform and select the “db8” Wavelet. The optimal combination of hyperparameters is $\lambda = 0.1, \eta = 0.1$ for all the values of ν .

⁷<https://deepinv.github.io/deepinv/>

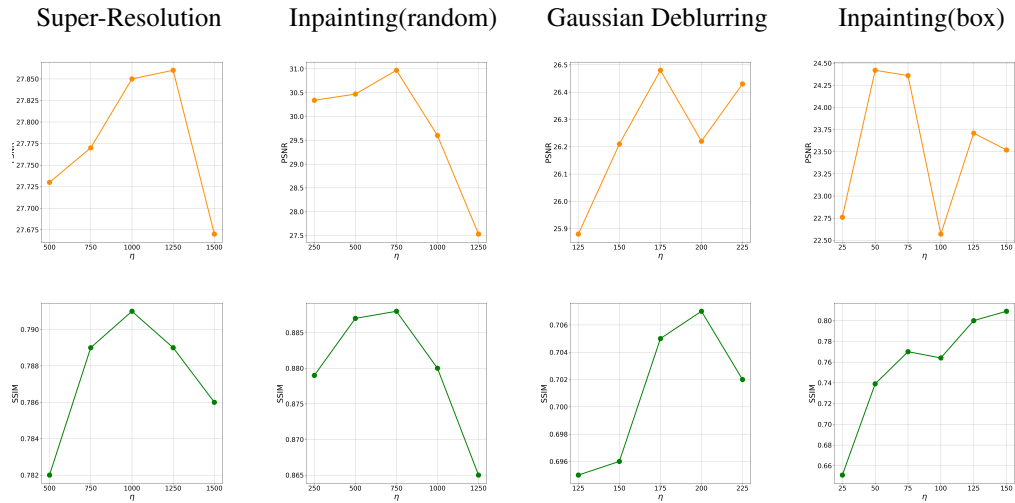


Figure 12: Hyperparameter η selection results for DPS-ODE. We select $\eta = 1000, 750, 200, 75$ for super-resolution, inpainting(random), Gaussian deblurring, and inpainting(box), respectively.

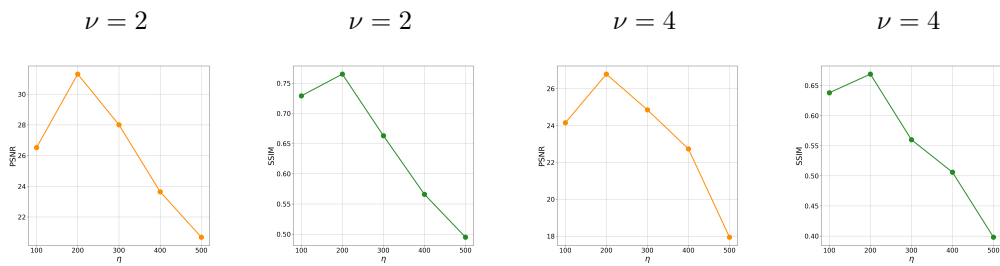


Figure 13: Hyperparameter η selection results for DPS-ODE on the HCP T2w dataset. We select $\eta = 200$ for all the experiments.